



TG, DSC, XRD, and SEM studies of the substituted lithium ferrite formation from milled $\text{Sm}_2\text{O}_3/\text{Fe}_2\text{O}_3/\text{Li}_2\text{CO}_3$ precursors

Elena N. Lysenko¹ · Vitaliy A. Vlasov¹ · Svetlana A. Nikolaeva¹ · Evgeniy V. Nikolaev¹

Received: 4 November 2021 / Accepted: 23 September 2022 / Published online: 10 October 2022
© Akadémiai Kiadó, Budapest, Hungary 2022

Abstract

Formation of substituted lithium ferrite $\text{Li}_{0.5}\text{Sm}_x\text{Fe}_{2.5-x}\text{O}_4$ (where $x = 0.06$ and 0.2) from $\text{Sm}_2\text{O}_3/\text{Fe}_2\text{O}_3/\text{Li}_2\text{CO}_3$ precursors was studied by X-ray diffraction analysis, thermogravimetry, differential scanning calorimetry, and scanning electron microscopy. The mixture of powders was subjected to preliminary mechanical activation in a planetary mill. We analyzed samples based on the precursors and synthesized at $900\text{ }^\circ\text{C}$ for 4 h in a laboratory furnace. It was found that ball milling of the precursors mixture in a planetary mill increases the powder reactivity. In spite of this, no substituted lithium ferrites were formed. It was shown that a two-phase composite that consists of pure lithium ferrite $\text{Li}_{0.5}\text{Fe}_{2.5}\text{O}_4$ and SmFeO_3 is formed during synthesis. An increase in the Sm_2O_3 content in the initial mixture provides an increase in the amount of the formed SmFeO_3 phase. The synthesis of $\text{Li}_{0.5}\text{Fe}_{2.5}\text{O}_4$ ferrite was confirmed by XRD analysis data, the Curie temperature ($627\text{--}630\text{ }^\circ\text{C}$) measured using TG analysis in a magnetic field, and by the presence of an endothermic peak on the DSC curve corresponding to the order–disorder transition in the $\text{Li}_{0.5}\text{Fe}_{2.5}\text{O}_4$ phase.

Keywords Lithium ferrite · Rare earth element · Samarium · Ball milling · Microstructure · Thermal analysis

Introduction

Good magnetic properties, including high Curie temperature and saturation magnetization, make it possible to use lithium ferrites in various microwave devices, in lithium-ion batteries as a cathode material, and in gas sensors [1–4]. It should be noted that lithium ferrites are of relatively low cost among the whole variety of ferrite materials.

Structural and electromagnetic properties of ferrites depend on both the chemical composition and the synthesis method [5–8]. Various methods of ferrite synthesis include sol–gel [9–11], combustion [12, 13], co-precipitation [14, 15], etc. However, a solid-state method using oxides and

carbonates is most widespread for producing lithium ferrites [16, 17]. Here, mechanical activation of the initial oxides can significantly accelerate and reduce the temperature of ferrite synthesis [18–22].

Properties of Li-ferrite substituted by various metal ions such as Ti, Zn, Ni, Mg, Mn, and Co were studied by many researchers [23–30]. This substitution made it possible to obtain ferrites of complex compositions with a specific combination of electrical and magnetic properties. However, ferrites of new compositions with unique properties are currently of increased interest [31].

Recent studies have focused on the properties of various ferrites with rare earth elements. It is known [32] that ions of rare earth elements have unpaired 4f electrons, which provide magnetic anisotropy due to their orbital shape. Magnetocrystalline anisotropy in ferrites is associated with the 4f–3d bond between transition metal ions and a rare earth element. Thus, doping of spinel ferrites with rare earth ions can improve their electrical and magnetic properties. In particular, such changes in the properties of ferrites occur when they are doped with gadolinium (Gd) [33–39], dysprosium (Dy) [37, 40–43], neodymium (Nd) [38, 44–46], samarium (Sm) [33, 47–51], lanthanum (La) [45, 52–54], terbium (Tb) [37, 40, 55–57], cerium (Ce) [33, 37, 58, 59], thulium (Tm)

✉ Svetlana A. Nikolaeva
sal17@tpu.ru

Elena N. Lysenko
lysenkoen@tpu.ru

Vitaliy A. Vlasov
vlvitan@tpu.ru

Evgeniy V. Nikolaev
nikolaev0712@tpu.ru

¹ Tomsk Polytechnic University, Lenina Avenue 30, Tomsk, Russia 634050

[60], erbium (Er) [37, 45, 47, 61, 62], holmium (Ho) [55, 63], ytterbium (Yb) [37], and praseodymium (Pr) [55].

As shown in [34, 35, 40, 64, 65], the introduction of rare earth elements, including Sm, is also of significant effect on the electromagnetic properties of lithium ferrites. In most studies, synthesis of ferrites with rare earth elements and their microstructural characteristics were investigated using X-ray diffraction analysis. It was suggested that substituted ferrites are formed with a small inclusion of secondary phases, for example, $GdFeO_3$ and $SmFeO_3$, depending on the doped rare earth element. Such phases affect the properties of the synthesized ferrites.

As shown in [40, 61, 63, 66, 67], thermal analysis methods provide more reliable data on the synthesis of ferrites with rare earth elements. Therefore, in this study, synthesis of lithium ferrite $Li_{0.5}Sm_xFe_{2.5-x}O_4$ from mechanically activated precursors $Sm_2O_3/Fe_2O_3/Li_2CO_3$ was investigated by X-ray diffraction (XRD), thermogravimetric (TG), and differential scanning calorimetric (DSC) analyses. The microstructure of the synthesized ferrite was examined using a scanning electron microscope (SEM).

Experimental

The procedure for preparing powders for synthesis included the following stages:

- Drying of precursors powders in a laboratory furnace at 200 °C for 180 min;
- Weighing of $Sm_2O_3/Fe_2O_3/Li_2CO_3$ powders (the ratio of the phase concentration is given in Table 1) using an analytical balance Shimadzu AUW-D to obtain proportions in accordance with the reactions:

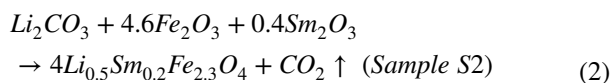
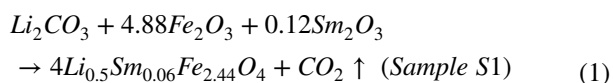


Table 1 Phase concentration of precursors

Sample	Phase composition	Phase concentration	
		mol%	mass%
S1	Li_2CO_3	16.7	8.2
	Fe_2O_3	81.3	87.1
	Sm_2O_3	2.0	4.7
S2	Li_2CO_3	16.7	7.8
	Fe_2O_3	76.7	77.5
	Sm_2O_3	6.6	14.7

- Additional sieving through a metal sieve with a mesh size of 100 μm ;
- Mechanical activation of powders mixtures in a planetary mill at 300 rpm for 15 min with steel grinding jars and balls. The mixture-to-ball mass ratio was 1:10;
- Pressing of the mechanically activated mixture using a hydraulic press at 200 MPa for 3 min.

After the above procedure for preparing powders, compacted samples S1 and S2 were synthesized at 900 °C for 240 min in air.

TG/DSC measurements were performed using a STA 449C Jupiter thermal analyzer with corundum crucibles. The heating rate was 10 °C min^{-1} . The formed phases of magnetic ferrite were additionally monitored by TG analysis in a magnetic field, the technique of which is described in [68, 69].

X-ray diffraction was performed using an ARL X'TRA diffractometer with CuK_{α} radiation. Qualitative and quantitative XRD analysis was performed using the PDF-4 + powder database of the International Center for Diffraction Data (ICDD). PowderCell 2.4 software was used to quantify phases, determine crystallite sizes using the Williamson–Hall method, and specify the lattice parameters. For quantitative XRD analysis, a set of experimental data obtained using a diffractometer was modeled by pseudo-Voigt profile function. The ultimate goal of this modeling is to obtain the best theory–experiment approximation.

The microstructure of the samples was investigated using a Hitachi TM-3000 scanning electron microscope.

Results and discussion

Thermal analysis of precursors and synthesized ferrites

In this study, a thermal analysis of the initial oxides used for ferrite synthesis was performed. TG/DSC analysis for iron oxide powder (not shown in this article) revealed no change in mass and significant calorimetric effects up to 800 °C. Only a small endothermic DSC peak at 677 °C associated with the magnetocaloric effect at the Néel temperature of $\alpha-Fe_2O_3$ was revealed.

Figure 1 shows the TG and DSC curves for the Sm_2O_3 and Li_2CO_3 precursors obtained in the heating mode in a thermal analyzer. For Sm_2O_3 , a three-step mass reduction occurs in the temperature range of 260–460 °C. However, the TG curve shows that the mass change is insignificant and, according to the data reported in [70], it is due to the loss of physically and chemically adsorbed water.

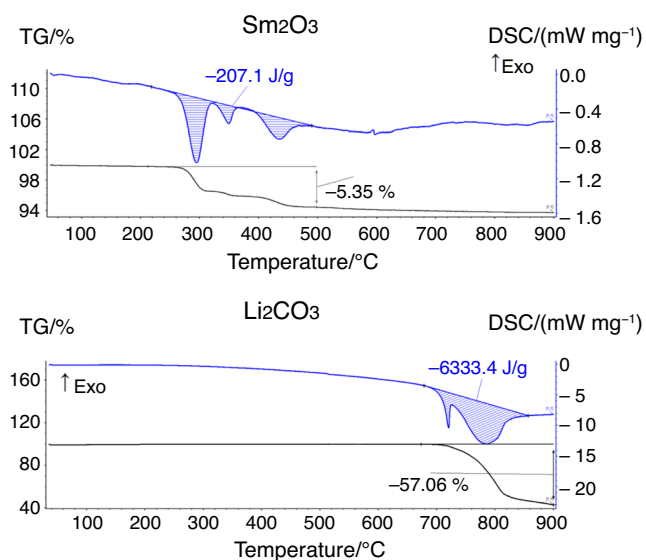


Fig. 1 TG/DSC curves of Sm_2O_3 and Li_2CO_3 raw reagents at heating regime

Thermal analysis of Li_2CO_3 lithium carbonate indicates that the mass changed near its melting point, which is known to vary within 720–735 °C. Therefore, the peaks on the DSC curve correspond to melting and decomposition of Li_2CO_3 with the release of carbon dioxide according to the reaction:



The total mass change on the TG curve equal to 57.06% and the enthalpy on the DSC curve equal to 245 kJ mol^{-1} for the release of CO_2 are close to the calculated values of 60% and 230 kJ mol^{-1} , respectively, in accordance with formula (3).

Thermal analysis of $\text{Sm}_2\text{O}_3/\text{Fe}_2\text{O}_3/\text{Li}_2\text{CO}_3$ precursors mixed in the ratio required to obtain samples S1 and S2 is illustrated in Figs. 2 and 3.

When unmilled powders are heated in the furnace of the thermal analyzer (Figs. 2a and 3a), the TG curve indicates a decrease in mass in several stages. The first stage in the temperature range of 280–450 °C, if compared with Fig. 1, is associated with the mass changes in Sm_2O_3 . The decreased mass (0.43 and 0.86% for samples S1 and S2, respectively) and the enthalpy of the associated heat effect for these samples correspond to the mass content of samarium oxide in the total mixture.

The change in mass in the temperature range of 470–700 °C is associated with the diffusion interaction between the reagents. The total mass loss in this temperature range is 5.01 and 4.59% for samples S1 and S2, respectively. These values are close to the expected ones of 4.92 and 4.64% for CO_2 release calculated from Eqs. (1) and (2), respectively. In [18], thermal analysis was used to study the

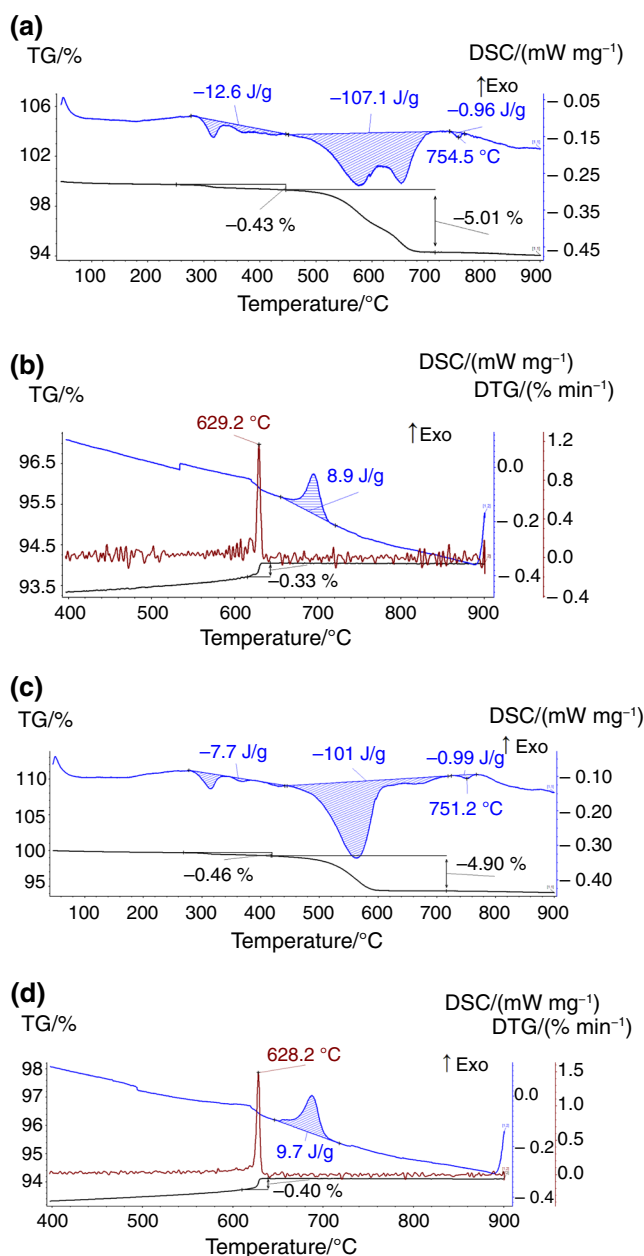


Fig. 2 TG/DTG/DSC curves at heating mode (a, c) and cooling mode in magnetic field (b, d) for S1 sample unmilled (a, b) and milled for 300 rpm (c, d)

synthesis reactions of lithium ferrites substituted by zinc and titanium. Mass spectrometric analysis of gasses showed only CO_2 release in this temperature range. The DSC peak indicates an endothermic peak with an enthalpy of 107 J g^{-1} for both samples close to the thermal effect of the interaction of iron oxide and lithium carbonate observed in [19].

It is known [18, 19] that mixing lithium carbonate with metal oxides accelerates the process of its decomposition. In particular, in a mixture with Fe_2O_3 , acceleration of the

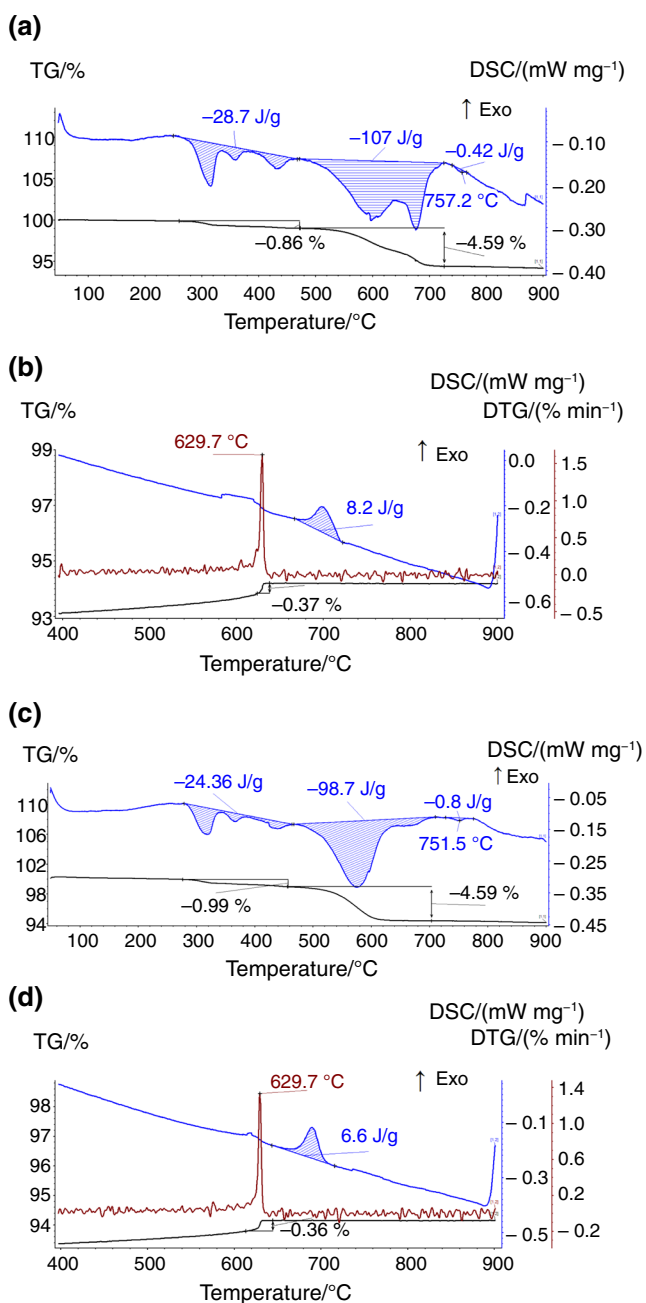


Fig. 3 TG/DTG/DSC curves at heating mode (a, c) and cooling mode in magnetic field (b, d) for S2 sample unmilled (a, b) and milled for 300 rpm (c, d)

lithium carbonate decomposition is associated with the predominant diffusion of Fe^{3+} cations into the Li_2CO_3 crystal lattice. Thus, Fig. 1 shows that the pure lithium carbonate decomposition begins at 700 °C. However, Figs. 2 and 3 illustrate a lower decomposition temperature for Li_2CO_3 with the release of CO_2 in the $\text{Sm}_2\text{O}_3/\text{Fe}_2\text{O}_3/\text{Li}_2\text{CO}_3$ mixture,

which is at least 250 °C lower than that for pure Li_2CO_3 . In this case, the reagents interact in two stages.

The study of the interaction between the Fe_2O_3 and Li_2CO_3 reagents to obtain lithium ferrites showed that the limiting stages of the reaction differ depending on the reaction temperature [19, 71]. At 500 °C and above, the reaction is mainly limited by diffusion interactions. However, in this case, the initial reaction product at low temperatures is lithium ferrite LiFeO_2 , regardless of the ratio of the initial components. With the initial molar ratio of Li_2CO_3 and Fe_2O_3 equal to 1:5 and a further increase in the temperature and duration of the synthesis, the reaction product is lithium ferrosphinel $\text{Li}_{0.5}\text{Fe}_{2.5}\text{O}_4$.

In this regard, a two-stage change in mass on the TG curve and a double peak on the DSC curve observed in Figs. 2a and 3a at 470–700 °C are associated with the formation of transition phases of lithium ferrite. This is evidenced by a small peak on the DSC curve at 750–760 °C, which is due to the order–disorder ($\alpha \rightarrow \beta$) phase transition in the formed $\text{Li}_{0.5}\text{Fe}_{2.5}\text{O}_4$ phase [18, 72]. The higher enthalpy of 0.96 J g^{-1} for sample S1 compared to the value of 0.42 J g^{-1} for sample S2 characterizes the higher ferrite content in sample S1 synthesized at the time of recording the DSC signal. This transition but with a higher intensity due to additional heating can similarly be observed on the DSC curve obtained at the cooling stage (Figs. 2b and 3b). The obtained enthalpy values of 8.9 J g^{-1} and 8.2 J g^{-1} for samples S1 and S2, respectively, are very close to the transition enthalpy for pure lithium ferrite with the DSC peak equal to 12 J g^{-1} [26].

Figures 2b and 3b demonstrate the results of TG analysis of the samples, when the magnets were attached immediately after the sample heating mode in accordance with the scheme proposed in [68]. The TG curves measured using a magnetic field show an abrupt increase in mass near the Curie temperature (T_c), which can be determined from the DTG curves. The T_c for samples S1 and S2 attains 629.2 and 629.7 °C, respectively, and these values are close to the temperature of the magnetic transition in ordered lithium ferrite with $T_c = 632 \text{ °C}$ [26, 68]. As reported in [72], a slight decrease in the Curie temperature of the samples can be associated with an increase in the degree of the order violation in the ferrite structure. In this case, this is apparently due to the addition of Sm_2O_3 .

Thus, the obtained results indicate the formation of a significant amount of unsubstituted lithium ferrite $\text{Li}_{0.5}\text{Fe}_{2.5}\text{O}_4$ during solid-phase interaction in the unmilled $\text{Sm}_2\text{O}_3/\text{Fe}_2\text{O}_3/\text{Li}_2\text{CO}_3$ mixture. Based on the results obtained, it is possible to estimate the content of lithium ferrite formed in the samples during thermal analysis. According to the

thermomagnetic methodology of ferrites presented in [68], the mass jump at the Curie temperature was observed to be 0.41% for pure lithium ferrite. As mentioned above, the enthalpy of $\alpha - \text{Li}_{0.5}\text{Fe}_{2.5}\text{O}_4$ to $\beta - \text{Li}_{0.5}\text{Fe}_{2.5}\text{O}_4$ transition according to the DSC analysis for pure lithium ferrite is 12 J g^{-1} [26]. Thus, the 0.33 and 0.37% in mass on TG curves as well as 8.9 and 8.2 J g^{-1} on DSC curves for samples S1 and S2, respectively, indicated that the ferrite content exceeds 70 mass% at the stage of cooling the mixture in a thermal analyzer.

The results of thermal analysis under non-isothermal heating of powders mechanically activated at 300 rpm are presented in Figs. 2c and 3c for samples S1 and S2, respectively. In such samples, a slight decrease in mass can also be observed at 280–450 °C, which is associated with mass changes in Sm_2O_3 . The higher values of mass change observed in this temperature range for both samples (0.46 and 0.99%), compared with the calculated values for the Sm_2O_3 content in the total mixture, are associated with the overlap of the temperature intervals of the processes occurring in Sm_2O_3 and the interaction between Fe_2O_3 and Li_2CO_3 .

The reaction of interaction between the milled $\text{Sm}_2\text{O}_3/\text{Fe}_2\text{O}_3/\text{Li}_2\text{CO}_3$ precursors with the release of CO_2 starts at a temperature of ca. 450 °C. The final temperature of the reaction is 700 °C. The total mass loss in this temperature range is 4.90% and 4.59% for samples S1 and S2, respectively. According to Eqs. (1) and (2), these values within experimental error are close to the calculated ones for the release of CO_2 . The behavior of the TG and DSC curves indicates that the synthesis reaction proceeds in two-stage with an enthalpy slightly lower than that of the reaction from non-activated powders. In this case, the main mass loss occurs in the first stage of the reaction up to 600 °C, which is 100 °C lower as compared to non-activated powders.

The enthalpies of $\alpha - \text{Li}_{0.5}\text{Fe}_{2.5}\text{O}_4$ to $\beta - \text{Li}_{0.5}\text{Fe}_{2.5}\text{O}_4$ phase transition, which are equal to 0.99 J g^{-1} and 0.8 J g^{-1} for samples S1 and S2, respectively, are higher than the values shown in Figs. 2a and 3a. This indicates the formation of a higher concentration of lithium ferrite in the milled samples during heating in thermal analyzer. Thus, mechanical activation of the reagent mixture accelerates the synthesis reaction between $\text{Sm}_2\text{O}_3/\text{Fe}_2\text{O}_3/\text{Li}_2\text{CO}_3$ precursors.

The results of TG analysis in a magnetic field presented in Figs. 2d and 3d reveal a high content of $\text{Li}_{0.5}\text{Fe}_{2.5}\text{O}_4$ lithium ferrite in both samples during solid-phase interaction in the mechanically activated $\text{Sm}_2\text{O}_3/\text{Fe}_2\text{O}_3/\text{Li}_2\text{CO}_3$ mixtures.

For milled sample S1, higher DSC peak of 9.7 J/g and the mass change of 0.4% indicate an increase in the lithium ferrite concentration during sample cooling in the thermal analyzer. However, the lower DSC peak of 6.6 J/g and the

mass change of 0.36% for milled sample S2 are apparently associated with a decrease in the amount of lithium ferrite due to the formation of other phase products such as SmFeO_3 , as shown below.

Figure 4 presents the results of thermal analysis obtained at the cooling stage for samples synthesized at 900 °C for 240 min from mechanically activated powders. According to the results of DSC analysis that show high values of the enthalpy of the $\beta - \text{Li}_{0.5}\text{Fe}_{2.5}\text{O}_4$ to $\alpha - \text{Li}_{0.5}\text{Fe}_{2.5}\text{O}_4$ phase transition, the synthesized samples contain mainly lithium ferrite $\text{Li}_{0.5}\text{Fe}_{2.5}\text{O}_4$. The content of this ferrite is higher in samples S1 compared to samples S2. No Curie temperatures connected to $\text{Li}_{0.5}\text{Sm}_{0.06}\text{Fe}_{2.44}\text{O}_4$ and $\text{Li}_{0.5}\text{Sm}_{0.2}\text{Fe}_{2.3}\text{O}_4$ phases were found.

X-ray diffraction analysis of synthesized ferrites

For a more comprehensive understanding of the processes that occur during the synthesis of ferrite, we performed XRD analysis of the samples synthesized at 900 °C for 240 min. Figure 5 shows XRD patterns for samples with different levels of doping with Sm^{3+} ions. It was found that some of the obtained peaks correspond to the cubic space group ($Fd-3m$). This indicates the formation of a spinel ferrite structure, namely, an ordered phase $\alpha - \text{Li}_{0.5}\text{Fe}_{2.5}\text{O}_4$

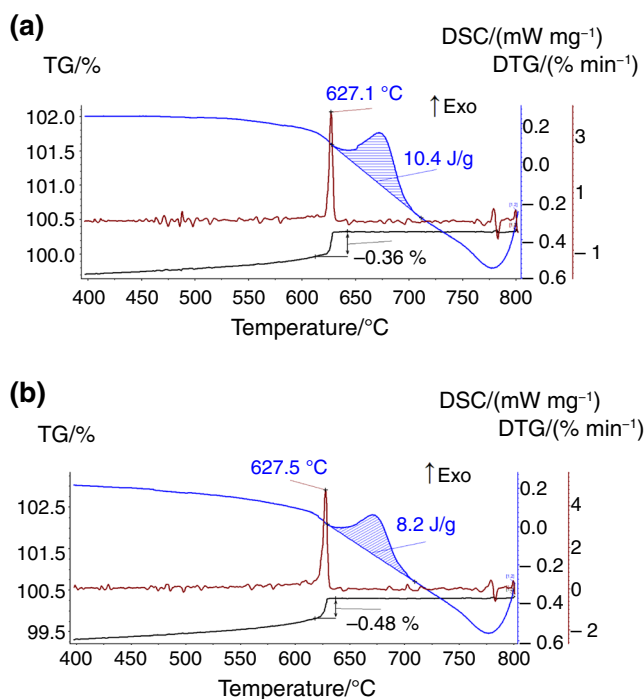


Fig. 4 TG/DTG/DSC curves at cooling mode in magnetic field for Sample S1 (a) and S2 (b) synthesized at 900 °C for 240 min

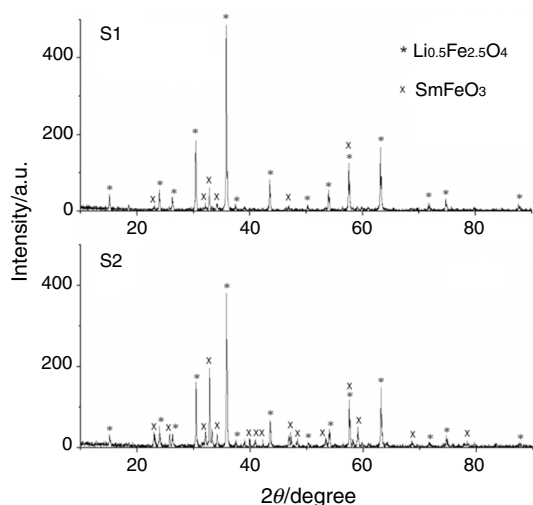


Fig. 5 X-ray diffraction of samples synthesized at 900 °C for 240 min

(PDF No. 04–015-5965). Yet, along with ferrite, a small amount of a crystalline secondary phase identified as SmFeO_3 is formed (PDF No. 00–039-1490) [65, 73]. It should be noted that SmFeO_3 is a non-magnetic material that exhibits an orthorhombic space group ($Pnma$). This phase can be formed as a result of the following reaction: $5\text{Fe}_2\text{O}_3 + 5\text{Sm}_2\text{O}_3 = 10\text{SmFeO}_3$.

Thus, the results of XRD analysis indicate the formation of a two-phase product based on $\text{Li}_{0.5}\text{Fe}_{2.5}\text{O}_4$ and SmFeO_3 in the process of solid-phase interaction. The quantitative content of phases is given in Table 2. At the same time, an increase in the Sm_2O_3 content from 4.7 to 14.7 mass% in the $\text{Sm}_2\text{O}_3/\text{Fe}_2\text{O}_3/\text{Li}_2\text{CO}_3$ mixture leads to an increase in the amount of the secondary phase SmFeO_3 from 4.9 to 17.5 mass% in synthesized samples. As shown in Table 2, the changed Sm_2O_3 content causes changes in the lattice constant.

Thus, for the synthesized samples, XRD and thermal analyses did not reveal the substituted phases of lithium ferrite, such as $\text{Li}_{0.5}\text{Sm}_{0.06}\text{Fe}_{2.44}\text{O}_4$ and $\text{Li}_{0.5}\text{Sm}_{0.2}\text{Fe}_{2.3}\text{O}_4$.

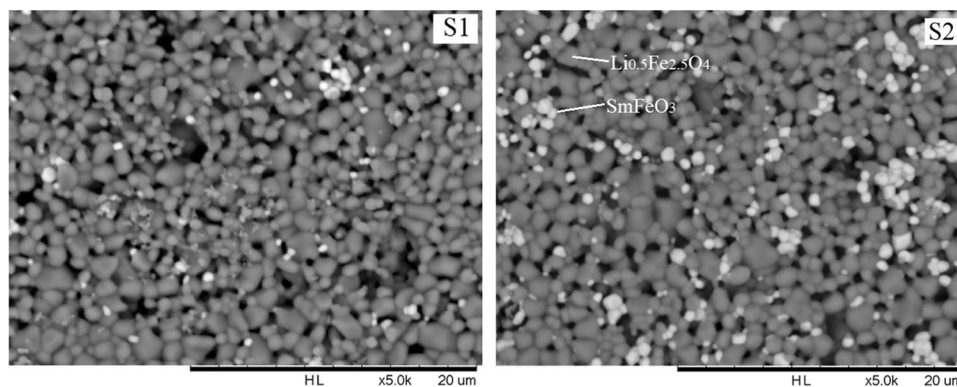
SEM analysis of synthesized samples

Figure 6 shows SEM images of the samples synthesized at 900 °C for 240 min. They demonstrate two distinct contrasts that presumably correspond to the ferrite phase (gray tint) and SmFeO_3 phase (white tint). Thus, the results obtained using SEM analysis confirm the conclusion drawn earlier on the formation of a two-phase product during the synthesis from the $\text{Sm}_2\text{O}_3/\text{Fe}_2\text{O}_3/\text{Li}_2\text{CO}_3$ powder mixture.

Table 2 X-ray diffraction data of ferrites synthesized at 900 °C for 240 min

Sample	Phase composition	Lattice parameter	Crystallite sizes	Phase concentration
		/Å	nm	mass%
S1	$\text{Li}_{0.5}\text{Fe}_{2.5}\text{O}_4$ SmFeO_3	$a=b=c=8.3297$	135	95.1
		$a=5.5921$; $b=7.7062$; $c=5.3999$	137	4.9
S2	$\text{Li}_{0.5}\text{Fe}_{2.5}\text{O}_4$ SmFeO_3	$a=b=c=8.3279$	170	82.5
		$a=5.5936$; $b=7.7046$; $c=5.3995$	45	17.5

Fig. 6 SEM micrographs of samples synthesized at 900 °C for 240 min



Conclusions

In this study, we examined the synthesis of lithium-substituted ferrite from mechanically activated $\text{Sm}_2\text{O}_3/\text{Fe}_2\text{O}_3/\text{Li}_2\text{CO}_3$ precursors using XRD, TG, DSC, and SEM analyses.

It was shown by thermal analysis that mechanical activation of the $\text{Sm}_2\text{O}_3/\text{Fe}_2\text{O}_3/\text{Li}_2\text{CO}_3$ mixture in a planetary mill increases the powder reactivity, so that the main reaction of reactants interaction occurs at lower temperatures. It was also found that the heating of the $\text{Sm}_2\text{O}_3/\text{Fe}_2\text{O}_3/\text{Li}_2\text{CO}_3$ mixture leads to the formation of a two-phase product that consists mainly of lithium ferrite $\text{Li}_{0.5}\text{Fe}_{2.5}\text{O}_4$ and the SmFeO_3 phase, the amount of which depends on the Sm_2O_3 content in the initial mixture. The synthesis of pure lithium ferrite was confirmed by XRD analysis data, the Curie temperature point, and by the presence of an endothermic peak on the DSC curve corresponding to the order–disorder transition in the $\text{Li}_{0.5}\text{Fe}_{2.5}\text{O}_4$ phase. The amount of lithium ferrite formed depends on the degree of powder milling. However, regardless of the mechanical activation of the powders, no substituted lithium ferrites such as $\text{Li}_{0.5}\text{Sm}_{0.06}\text{Fe}_{2.44}\text{O}_4$ and $\text{Li}_{0.5}\text{Sm}_{0.2}\text{Fe}_{2.3}\text{O}_4$ were formed.

It is known that unsubstituted lithium ferrite with the chemical composition of $\text{Li}_{0.5}\text{Fe}_{2.5}\text{O}_4$ is not used in microwave technology due to high dielectric losses. However, this ferrite has the high values of saturation magnetization and Curie temperature. It can be assumed that the formation of $\text{Li}_{0.5}\text{Fe}_{2.5}\text{O}_4/\text{SmFeO}_3$ composite structure can primarily affect the electrical properties of ferrites. In this regard, this work needs to be continued in terms of studying the electrical and magnetic properties of synthesized ferrites.

Acknowledgments The research was supported by RFBR grant (project No. 20-07-00662). The experiments were supported by the Tomsk Polytechnic University development program.

References

- Sláma J, Šoka M, Grusková A, Dosoudil R, Jančárik V, Degmová J. Magnetic properties of selected substituted spinel ferrites. *Magn Magn Mater.* 2013;326:251–6.
- Zhang Q, Song J, Wang L. Lithium-zinc-ferrite microwave electromagnetic consumable material and preparation method thereof. China Patent No. 2010. 101696106.
- Ahniyaz A, Fujiwara T, Song S-W, Yoshimura M. Low temperature preparation of β - LiFe_5O_8 fine particles by hydrothermal ball milling. *J Solid State Ionics.* 2002;151:419–23.
- Rezlescu N, Doroftei C, Rezlescu E, Popa PD. Lithium ferrite for gas sensing applications. *Sens Actuat B.* 2008;133:420–5.
- Ștefănescu M, Dippong T, Stoia M, Ștefănescu O. Study on the obtaining of cobalt oxides by thermal decomposition of some complex combinations, undispersed and dispersed in SiO_2 matrix. *J Therm Anal Calorim.* 2008;94:389–93. <https://doi.org/10.1007/s10973-008-9111-2>.
- Dippong T, Levei EA, Borodi G, Goga F, Barbu TL. Influence of Co/Fe ratio on the oxide phases in nanoparticles of $\text{Co}_x\text{Fe}_{3-x}\text{O}_4$. *J Therm Anal Calorim.* 2015;119:1001–9. <https://doi.org/10.1007/s10973-014-4280-7>.
- Barvinschi P, Stefanescu O, Dippong T, Sorescu S, Stefanescu M. $\text{CoFe}_2\text{O}_4/\text{SiO}_2$ nanocomposites by thermal decomposition of some complex combinations embedded in hybrid silica gels. *J Therm Anal Calorim.* 2013;112:447–53. <https://doi.org/10.1007/s10973-012-2704-9>.
- Kammar EA, Gad EAM, Mousa MA. Kinetics of thermal decomposition of ammonium perchlorate with nanocrystals of $\text{Ni}_x\text{Co}_{1-x}\text{Fe}_2\text{O}_4$ ($x = 0, 0.05, \text{ and } 1$) ferrites. *J Therm Anal Calorim.* 2021. <https://doi.org/10.1007/s10973-021-11112-7>.
- Dippong T, Levei EA, Cadar O, Goga F, Borodi G, Barbu-Tudoran L. Thermal behavior of $\text{Co}_x\text{Fe}_{3-x}\text{O}_4/\text{SiO}_2$ nanocomposites obtained by a modified sol–gel method. *J Therm Anal Calorim.* 2017;128:39–52. <https://doi.org/10.1007/s10973-016-5930-8>.
- An SY, Shim IB, Kim CS. Synthesis and magnetic properties of LiFe_5O_8 powders by a sol–gel process. *Magn Magn Mater.* 2005;290–291:1551–4. <https://doi.org/10.1016/j.jmmm.2004.11.244>.
- Asif Iqbal M, Islam MU, Ali I, Khan MA, Sadiq I, Ali I. High frequency dielectric properties of Eu^{3+} -substituted Li–Mg ferrites synthesized by sol–gel auto-combustion method. *J Alloys Compd.* 2014;586:404–10.
- Gupta M, Randhawa BS. Microstructural, magnetic and electric properties of mixed Cs–Zn ferrites prepared by solution combustion method. *Sol St Sci.* 2012;14:849–56.
- Dessai PPG, Verenkar VMS. Synthesis and characterization of $\text{Ni}_{0.7-x}\text{Mn}_x\text{Zn}_{0.3}\text{Fe}_2(\text{C}_4\text{H}_2\text{O}_4)_3 \cdot 6\text{N}_2\text{H}_4$ ($x = 0.1–0.6$): a precursor for the synthesis of nickel manganese zinc ferrites. *J Therm Anal Calorim.* 2020;142:1399–411.
- Ali I, Islam MU, Ishaque M, Khan HM, Naeem Ashiq M, Rana MU. Structural and magnetic properties of holmium substituted cobalt ferrites synthesized by chemical co-precipitation method. *Magn Magn Mater.* 2012;324:3773–7.
- Shinde BL, Mandle UM, Pachpinde AM, Lohar KS. Synthesis and characterization of Al^{3+} substituted Ni–Cu–Zn nano ferrites. *J Therm Anal Calorim.* 2021;147(4):2947–56. <https://doi.org/10.1007/s10973-021-10719-0>.
- Zhu X, Cao C, Shubing S, Xia A, Zhang H, Li H, Liu Z, Jin C. A comparative study of spinel ZnFe_2O_4 ferrites obtained via a hydrothermal and a ceramic route: structural and magnetic properties. *Ceram Int.* 2021;47(11):15173–9. <https://doi.org/10.1016/j.ceramint.2021.02.077>.
- Thakur P, Chahar D, Taneja S, Bhalla N, Thakur A. A review on MnZn ferrites: synthesis, characterization and applications. *Ceram Int.* 2020;46:15740–63.
- Lysenko EN, Surzhikov AP, Vlasov VA, Malyshev AV, Nikolaev EV. Thermal analysis study of solid-phase synthesis of zinc- and titanium-substituted lithium ferrites from mechanically activated reagents. *J Therm Anal Calorim.* 2015;122:1347–53. <https://doi.org/10.1007/s10973-015-4849-9>.
- Lysenko EN, Nikolaev EV, Surzhikov AP, Nikolaeva SA, Plotnikova IV. The influence of reagents ball milling on the lithium ferrite formation. *J Therm Anal Calorim.* 2019;138:2005–13. <https://doi.org/10.1007/s10973-019-08334-1>.
- Berbenni V, Marini A, Matteazzi P, Ricceri R, Welham N. Solid-state formation of lithium ferrites from mechanically activated $\text{Li}_2\text{CO}_3\text{-Fe}_2\text{O}_3$ mixtures. *J Eur Ceram Soc.* 2003;23:527–36. [https://doi.org/10.1016/S0955-2219\(02\)00150-4](https://doi.org/10.1016/S0955-2219(02)00150-4).
- Chen D, Harward I, Baptist J, Goldman S, Celinski Z. Curie temperature and magnetic properties of aluminum doped barium ferrite particles prepared by ball mill method. *Magn Magn Mater.* 2015;395:350–3. <https://doi.org/10.1016/j.jmmm.2015.07.076>.

22. Widatallah HM, Berry FJ. The influence of mechanical milling and subsequent calcination on the formation of lithium ferrites. *J Solid State Chem.* 2002;164:230–6. <https://doi.org/10.1006/jssc.2001.9466>.
23. Lysenko E, Nikolaev E, Vlasov V, Surzhikov A. Microstructure and reactivity of $\text{Fe}_2\text{O}_3\text{-Li}_2\text{CO}_3\text{-ZnO}$ ferrite system ball-milled in a planetary mill. *Thermochim Acta.* 2018;664:100–7. <https://doi.org/10.1016/j.tca.2018.04.015>.
24. Teixeira SS, Graça MPF, Costa LC. Dielectric, morphological and structural properties of lithium ferrite powders prepared by solid state method. *J Non-Cryst Sol.* 2012;358:1924–9.
25. Shahjahan M, Ahmed NA, Rahman SN, Islam S. Structural and electrical characterization of Li-Zn ferrites. *Int J Inn Tech Exp Eng.* 2014;3(8):48–52.
26. Lysenko EN, Malyshev AV, Vlasov VA, Nikolaev EV, Surzhikov AP. Microstructure and thermal analysis of lithium ferrite pre-milled in a high-energy ball mill. *J Therm Anal Calorim.* 2018;134:127–33.
27. Verma S, Karande J, Patidar A, Joy PA. Low-temperature synthesis of nanocrystalline powders of lithium ferrite by an autocombustion method using citric acid and glycine. *Mat Lett.* 2005;59:2630–3.
28. Aravind G, Raghasudha M, Ravinder D, Manivel Raja M, Meena SS, Bhatt P, Hashim M. Study of structural and magnetic properties of Li-Ni nanoferrites synthesized by citrate-gel auto combustion. *Ceram Int.* 2016;42:2941–50.
29. Vijaya Bhasker Reddy P, Ramesh B, Gopal RC. Electrical conductivity and dielectric properties of zinc substituted lithium ferrites prepared by sol gel method. *Physica B.* 2010;405:1852–6.
30. Nikolaev EV, Lysenko EN, Surzhikov AP, Ghyngazov SA, Bordunov SV, Nikolaeva SA. Dilatometric and kinetic analysis of sintering Li-Zn ferrite ceramics from milled reagents. *J Therm Anal Calorim.* 2020;142:1783–9.
31. Nikolaeva SA, Lysenko EN, Nikolaev EV, Surzhikov AP. Dilatometric analysis of sintering lithium-titanium-zinc ferrite with ZrO_2 additive. *J Therm Anal Calorim.* 2022;147:1091–6. <https://doi.org/10.1007/s10973-020-10416-4>.
32. Khan MA, Sabir M, Mahmood A, Asghar M, Mahmood K, Khan MA, Ahmad I, Sher M, Warsi MF. High frequency dielectric response and magnetic studies of $\text{Zn}_{1-x}\text{Tb}_x\text{Fe}_2\text{O}_4$ nanocrystalline ferrites synthesized via micro-emulsion technique. *Magn Magn Mater.* 2014;360:188–92.
33. Zhong XC, Guo XJ, Zou SY, Yu HY, Liu ZW, Zhang YF, Wang KX. Improving soft magnetic properties of Mn-Zn ferrite by rare earth ions doping. *AIP Adv.* 2018;8:047807.
34. Jiang J, Liangchao L, Feng X. Structural analysis and magnetic properties of Gd-doped Li-Ni ferrites prepared using rheological phase reaction method. *J Rare Earths.* 2007;25:79–83.
35. Gajula GR, Buddiga LR. Structural, ferroelectric, dielectric, impedance and magnetic properties of Gd and Nb doped barium titanate-lithium ferrite solid solutions. *Magn Magn Mater.* 2020;494:165822.
36. Zhao LJ, Yang H, Yu LX, Cui YM, Feng SH. Effects of Gd_2O_3 on structure and magnetic properties of Ni-Mn ferrite. *J Mater Sci.* 2006;41:3083–7.
37. Rezlescu E, Rezlescu N, Popa PD, Rezlescu L, Pasnicu C. The influence of R_2O_3 (R = Yb, Er, Dy, Tb, Gd, Sm and Ce) on the electric and mechanical properties of a nickel-zinc ferrite. *Phys Status Solidi A.* 1997;162:673–8.
38. Nikumbh AK, Pawar RA, Nighot DV, Gugale GS, Sangale MD, Khanvilkar MB, Nagawade AV. Structural, electrical, magnetic and dielectric properties of rare-earth substituted cobalt ferrites nanoparticles synthesized by the co-precipitation method. *Magn Magn Mater.* 2014;355:201–9.
39. Heiba ZK, Bakr Mohamed M, Arda L, Dogan N. Cation distribution correlated with magnetic properties of nanocrystalline gadolinium substituted nickel ferrite. *Magn Magn Mater.* 2015;391:195–202.
40. Junaid M, Khan MA, Iqbal F, Murtaza G, Akhtar MN, Ahmad M, Shakir I, Warsi MF. Structural, spectral, dielectric and magnetic properties of Tb-Dy doped Li-Ni nano-ferrites synthesized via micro-emulsion route. *Magn Magn Mater.* 2016;419:338–44.
41. Naik S, Salker A. Change in the magnetostructural properties of rare earth doped cobalt ferrites relative to the magnetic anisotropy. *J Mater Chem.* 2012;22:2740–50.
42. Slimani Y, Almessiere MA, Güner S, Kurtan U, Shirsath SE, Baykal A, Ercan I. Magnetic and microstructural features of Dy^{3+} substituted NiFe_2O_4 nanoparticles derived by sol-gel approach. *J Sol-Gel Sci Techn.* 2020;95:202–10.
43. Li DY, Sun YK, Xu Y, Ge HL, Wu Q, Yan C. Effects of Dy^{3+} substitution on the structural and magnetic properties of $\text{Ni}_{0.5}\text{Zn}_{0.5}\text{Fe}_2\text{O}_4$ nanoparticles prepared by a sol-gel self-combustion method. *Ceram Int.* 2015;41:4581–9.
44. Naik PP, Tangsali RB, Meena SS, Yusuf SM. Influence of rare earth (Nd^{3+}) doping on structural and magnetic properties of nanocrystalline manganese-zinc ferrite. *Mater Chem Phys.* 2017;191:215–24.
45. Wei J, Wu CF, Liu YL, Guo YX, Yang TT, Wang DW, Xu Z, Hautmont R. Structural distortion, spin-phonon coupling, interband electronic transition, and enhanced magnetization in rare-earth-substituted bismuth ferrite. *Inorg Chem.* 2017;56:8964–74.
46. Eltabey MM, Agami WR, Mohsen HT. Improvement of the magnetic properties for Mn-Ni-Zn ferrites by rare earth Nd^{3+} ion substitution. *J Adv Res.* 2014;5:601–5.
47. Boda N, Boda G, Naidu KCB, Srinivas M, Batoo KM, Ravinder D, Reddy AP. Effect of rare earth elements on low temperature magnetic properties of Ni and Co-ferrite nanoparticles. *Magn Magn Mater.* 2019;473:228–35.
48. Alikin DO, Turygin AP, Walker J, Bencan A, Malic B, Rojac T. The effect of phase assemblages, grain boundaries and domain structure on the local switching behavior of rare-earth modified bismuth ferrite ceramics. *Acta Mater.* 2017;125:265–73.
49. Falsafi F, Hashemi B, Mirzaei A, Fazio E, Neri F, Donato N, Leonardi SG, Neri G. Sm-doped cobalt ferrite nanoparticles: a novel sensing material for conductometric hydrogen leak sensor. *Ceram Int.* 2017;43:1029–37.
50. Taneja S, Thakur P, Ravelo B, Thakur A. Nanocrystalline samarium doped nickel-zinc-bismuth ferrites: investigation of structural, electrical and dielectric properties. *Mater Res Bull.* 2022;154:111937. <https://doi.org/10.1016/j.materresbull.2022.111937>.
51. Keerthana SP, Yuvakkumar R, Senthil Kumar P, Ravi G, Velauthapillai D. Rare earth metal (Sm) doped zinc ferrite (ZnFe_2O_4) for improved photocatalytic elimination of toxic dye from aquatic system. *Envir Res.* 2021;197:111047. <https://doi.org/10.1016/j.envres.2021.111047>.
52. Channagoudra G, Peter J, Nunez J, Hadimani Ravi L, Dayal V. Study of cation distribution in La^{3+} and Eu^{3+} substituted cobalt ferrite and its effect on magnetic properties. *Magn Magn Mater.* 2022;5591:169550. <https://doi.org/10.1016/j.jmmm.2022.169550>.
53. Guo H-S, Zhang L, Yan Y-L, Zhang J, Wang J, Wang S-Y, Li L-Z, Wu X-H. Effect of lanthanum substitution on structural, magnetic, and electric properties of Ni-Zn-Co ferrites for radio frequency and microwave devices. *Ceram Int.* 2022;15:22557–631. <https://doi.org/10.1016/j.ceramint.2022.04.275>.
54. Abdel Maksoud MIA, El-Ghandour A, Ashour AH, Atta MM, Abdelhaleem S, El-Hanbaly AH, Fahim RA, Kassem SM, Shalaby MS, Awed AS. La^{3+} doped $\text{LiCo}_{0.25}\text{Zn}_{0.25}\text{Fe}_2\text{O}_4$ spinel ferrite

- nanocrystals: insights on structural, optical and magnetic properties. *J Rare Earths*. 2021;39:75–82.
55. Alikin DO, Turygin AP, Walker J, Bencan A, Malic B, Rojac T, Shur VY, Kholkin AL. Effect of the rare-earth substitution on the structural, magnetic and adsorption properties in cobalt ferrite nanoparticles. *Ceram Int*. 2016;42:4246–55.
 56. Jacob BP, Thankachan S, Xavier S, Mohammed EM. Effect of Tb³⁺ substitution on structural, electrical and magnetic properties of sol–gel synthesized nanocrystalline nickel ferrite. *J Alloys Compd*. 2013;578:314–9.
 57. Sadaqat A, Almessiere M, Slimani Y, Guner S, Sertkol M, Albetran H, Baykal A, Shirsath SE, Ozcelik B, Ercan I. Structural, optical and magnetic properties of Tb³⁺ substituted Co nanoferrites prepared via sonochemical approach. *Ceram Int*. 2019;45:22538–46.
 58. Ahmad SL, Ansari SA, Ravi KD. Structural, morphological, magnetic properties and cation distribution of Ce and Sm co-substituted nano crystalline cobalt ferrite. *Mater Chem Phys*. 2018;208:248–57.
 59. Hu J, Li Z, Yu H, Zhong X, Liu Z, Long K, Li J. Modifying the soft magnetic properties of Mn-Zn ferrites by Ce₂O₃-doping and sintering temperature optimization. *J Elect Mat*. 2020;49:6501–9.
 60. Almessiere MA, Slimani Y, Kurtan U, Guner S, Sertkol M, Shirsath SE, Akhtar S, Baykal A, Ercan I. Structural, magnetic, optical properties and cation distribution of nanosized Co_{0.7}Zn_{0.3}TmxFe_{2-x}O₄ (0.0≤x≤0.04) spinel ferrites synthesized by ultrasonic irradiation. *Ultrason Sonochem*. 2019;58:104638.
 61. Noreen Z, Ahmad I, Siddiqui F, Ziya AB, Abbas T, Bokhari H. Size dependent structural, anti-bacterial and anti-biofilm properties of Er doped Li-Ni ferrites synthesized by the sol–gel auto-combustion route. *Ceram Inter*. 2017;43:10784–90.
 62. Rajashekar K, Vinod G, Mahesh Kumar K, Naik JL. Impact of erbium (Er) doping on the structural and magnetic properties of Ni-Cu (Ni_{0.1}Cu_{0.9}Fe₂O₄) nanoferrites. *Magn Magn Mater*. 2022;5551:169323. <https://doi.org/10.1016/j.jmmm.2022.169323>.
 63. Manzoor A, Khan MA, Khan MY, Akhtar MN, Hussain A. Tuning magnetic and high frequency dielectric behavior in Li-Zn ferrites by Ho doping. *Ceram Int*. 2018;44:6321–9.
 64. Li L, Jiang J, Xu F. Synthesis and ferrimagnetic properties of novel Sm-substituted LiNi ferrite-polyaniline nanocomposite. *Mater Lett*. 2007;61:1091–6.
 65. Mahmoudi M, Kavanlouei M, Maleki-Ghaleh H. Effect of composition on structural and magnetic properties of nanocrystalline ferrite Li_{0.5}Sm_xFe_{2.5-x}O₄. *Powd Metal Metal Ceram*. 2015;54:31–9.
 66. Ashour AH, Hemeda OM, Heiba ZK, Al-Zahrani SM. Electrical and thermal behavior of PS/ferrite composite. *Magn Magn Mater*. 2014;369:260–7.
 67. AsifIqbal M, Islam MU, Ali I, Azhar Khan M, Ramay SM, Hassan Khan M, Khalid MM. Study of physical, magnetic and electrical properties of rare-earth substituted Li-Mg ferrites. *J Alloys Compd*. 2017;692:322–31.
 68. Lysenko EN, Surzhikov AP, Astafyev AL. Thermomagneto-metric analysis of lithium ferrites. *J Therm Anal Colorim*. 2019;136:441–5.
 69. Lysenko EN, Astafyev AL, Vlasov VA, Surzhikov AP. Analysis of phase composition of LiZn and LiTi ferrites by XRD and thermomagneto-metric analysis. *J Magn Magn Mater*. 2018;465:457–61.
 70. Yousefi T, Mostaeidi MT, Ghasemi M, Ghadirifar A. A Simple Way to Synthesize of Samarium Oxide Nanoparticles: Characterization and Effect of pH on Morphology. *Synth React Inorg Met-Org Nano-Met Chem*. 2016;46:137–42. <https://doi.org/10.1080/15533174.2014.900795>.
 71. Lysenko EN, Nikolaev EV, Vasendina EA. Investigation of heating rate effect on solid-phase interaction in Li₂CO₃–Fe₂O₃ reaction mixture. *IOP Conf Ser Mater Sci Eng*. 2015;81:012104. <https://doi.org/10.1088/1757-899X/81/1/012104>.
 72. Surzhikov AP, Frangulyan TS, Ghyngazov SA, Lysenko EN. Investigation of structural states and oxidation processes in Li_{0.5}Fe_{2.5}O_{4-δ} using TG analysis. *J Therm Anal Calorim*. 2012;108:1207–12.
 73. Inbanathan SSR, Vaithyanathan V, Arout Chelvane J, Markandeyulu G, Kamala BK. Mössbauer studies and enhanced electrical properties of R (R=Sm, Gd and Dy) doped Ni ferrite. *Magn Magn Mater*. 2014;353:41–6.

Publisher's Note Springer Nature remains neutral with regard to jurisdictional claims in published maps and institutional affiliations.

Springer Nature or its licensor holds exclusive rights to this article under a publishing agreement with the author(s) or other rightsholder(s); author self-archiving of the accepted manuscript version of this article is solely governed by the terms of such publishing agreement and applicable law.